An experimental study on the strain-rate-dependent compressive and tensile response of an alumina ceramic

Min Ji[a], Haoyang Li[a], Jie Zheng[a], Shuo Yang[a], Zahra Zaiemyekeh[a], James D. Hogan[a,*]

[a]Department of Mechanical Engineering, University of Alberta, Edmonton, AB T6G 2R3, Canada

Abstract

This research article studied the strain-rate-dependent mechanical response of a CeramTec Alotec 98% alumina ceramic under uniaxial compression and indirect tension loadings. Mechanical testing was carried out using a load frame for quasi-static strain rates and a split-Hopkinson Pressure Bar (SHPB) for dynamic strain rates combined with the digital image correlation (DIC) technique and ultra-high-speed photography to investigate strain-rate-dependent failure behavior. Furthermore, scanning electron microscopy coupled with energy-dispersive X-ray spectroscopy, electron backscatter diffraction, and X-ray microscopy was applied to determine the microstructural and failure features before and after experiments (e.g., elemental composition, grain size, voids, and impurities). Experimental results showed that the strength in compression was $>10\times$ higher than those in tension. In addition, a strain-rate-sensitivity of strength on compression (linear fit slope of 0.68) was greater than in tension (0.39), and this was believed to be associated with crack growth and interaction, manifested as differences in measured crack speeds between the compression (2.5 ± 1.3 km/s) and tension (5.9 ± 2.1 km/s). Post-mortem analysis of fracture surfaces revealed that intergranular fracture was more likely to appear in quasi-static loading and transgranular fracture in dynamic loading loading in alumina, with compression generating more micro-cracks as expected. Overall, this paper provides new comparative strain-rate-dependent strength and crack speed measurements of compression and tension, which serve as important inputs for future computational/numerical model development and validation.

Keywords: Alumina ceramic, Strain-rate-dependent, Uniaxial compression experiments, Indirect tension experiments, SHPB, Failure mechanisms

*Corresponding author
  Email address: jdhogan@ualberta.ca (James D. Hogan)

1. Introduction

Aluminum oxide (alumina) ceramic, with a favorable combination of properties including high strength-to-weight ratio, high hardness, and low density is attractive for use in engineering applications such as protection, aerospace, and nuclear systems [1–3]. As a type of brittle material, alumina undergoes fracture when experiencing impact or blast loads [2, 4], and therefore, studies on alumina ceramics have focused on the mechanical response and failure modes under various mechanical loading conditions [2, 5–8]. In addition, the microstructural features of the materials including grain size, pores, and impurities have also been reported to have a strong relationship with properties, and failure mechanisms, (e.g., serving as potential crack nucleation sites [3, 9]). To date, a key area of research has focused on better understanding how the mechanical properties such as compressive and tensile strength are influenced by strain rate. The majority of the literatures of brittle materials are focused on studying compressive mechanical properties related to the microstructure (grain size, voids and impurities distributions [10, 11]) and strain rate [1, 5, 12, 13]. For instance, Lankford et al. [6] investigated the mechanisms responsible for the strain-rate-dependent compressive strength in ceramics, and the strain-rate sensitivity of strength was attributed to both material-dependent mechanisms activated at $\sim 10^2$ s^{-1} and inertia-dependent processes at higher strain rates. In another study, Wang et al. [14] studied the effect of the strain rate on the failure strength of alumina. The results showed a sensitivity of strength to high strain rates (> 250 s^{-1}), as distinguished from the lower strain-rate regime, with a power law formula used to quantify the strain rate dependency. More recently, Koch et al. [3] investigated the relationship between microstructure, crack speeds, and mechanical properties of alumina ceramics, and they found that lower purity alumina was less able to resist impact. Based on these experiments and others conducted in the literature [2, 15, 16], the strain-rate sensitivity of alumina ceramics has been attributed to the growth of axial cracks [5, 6].

While many studies have focused on the compressive response of advanced ceramics [5, 6, 17], limited efforts have been made to study the tensile response [8, 18]. This may be due to difficulties in generating/forming the ideal state of uniaxial tension (e.g., dog-bone test) [14], and obtaining an ideal state of uniaxial tension in the tested sample under static and/or dynamic conditions [19]. As an alternative, the Brazilian disk (indirect tension) test using a split-Hopkinson pressure bar (SHPB) technique has become a popular method to determine tensile strength for brittle materials such as rocks [20], glasses [15, 21], and some ceramics [14, 22]. The Brazilian disk experiment was first introduced by the International Society for Rock Mechanics (ISRM) [23] as a standard method to investigate the tensile properties of rocks (e.g., strength). This method applies a compressive loading in the axial direction to induce an indirect tensile stress state on disk-shaped samples, eventually resulting in failure by the formation of a spanwise-propagating crack originating from the center of the disk [4]. In one study, involving Brazilian disk testing, Glavez et al. [8] studied the tensile strength using a split-Hopkinson pressure bar to achieve strain rates up to $\sim 10^2$ s^{-1} on

alumina with different purities (i.e., 94%, 98% and 99.5%), and they found an increase in strength sensitivity to strain rate. Still, it remains a challenge to produce a uniform stress and strain distribution using an SHPB as a result of the brittleness of ceramic materials, which requires a modification (e.g., using pulse shaper) on the SHPB system and sample geometry [21]. Further, Swab et al. [24] noted that the tensile strength of a magnesium aluminate ceramic was challenging to determine in the diametral compression (Brazilian disk) tests because the fracture process initiated at the loading interfaces. In their study, Swab et al. [24] noted that a more valid experiment occurred when the crack initiated at the center of the disk, and this was also a key criteria reported earlier by Wang et al. [25]. In the Wang et al. [25] study, they improved the Brazilian disk tests by designing the Flattened Brazilian disk (FBD) sample with two small parallel planes at the surface of the specimen contacting the SHPB bars, providing a more uniform stress distribution during the loading process. The FBD tests were also adopted by many researchers on various brittle materials (e.g., ceramic [18], glass [24], and rock [4]), and they found that parallel surfaces reduce the stress concentration at the loading edge, which further improved the test validity [26].

Altogether, studying both the compressive and tensile responses of a brittle material at different strain rates are critical because: 1. understanding the strain-rate-dependent behavior is prevalent for materials to be used in dynamic loading environments [5, 27]; 2. the properties extracted under both compressive and tensile states (e.g., strength, Young's modulus) are essential parameters in almost all constitutive models to describe material behavior (e.g., the Johnson-Holmquist models [17]); and 3. the ability to qualitatively and quantitatively describe the fracture behavior (e.g., crack speed [28]) is important for generating new insights needed to develop stress-state- and strain-rate-dependent damage evolution models [19, 29]. To date, few studies investigated both compressive and tensile properties for brittle materials across a wide range of strain rates. For example, Gao et al. (10^{-3} s^{-1} to 723 s^{-1} for compression experiments and 10^{-3} s^{-1} to 265 s^{-1} for indirect tension experiments), Ross et al. (10^{-7} s^{-1} to 300 s^{-1} for compression experiments and $\sim$ 5.8 s^{-1} for indirect tension experiments), and Yang et al. (7.3 s^{-1} to 72.7 s^{-1} for compression experiments and 1.0 s^{-1} to 5.9 s^{-1} for indirect tension experiments) investigated both stress states with strain rate ranges noted in the brackets. In the current study, we provide complete data sets for both tensile and compressive stress states and cover a wider range of strain rates through established pulse shaping techniques developed in the authors' research group [30, 31] Specifically, in this study, we investigate the strain-rate-dependent mechanical properties (e.g., strength, failure strain) and failure (e.g., crack speeds, fracture modes) of a CeramTec Alotec 98% alumina ceramic using both uniaxial compression and indirect tension approaches. First, electron backscattered diffraction (EBSD) techniques and X-ray computed tomography (XCT) were used to characterize the grain morphology and quantify the impurities and porosity of the material. In addition, scanning electron microscopy (SEM) equipped with energy dispersion spectroscopy (EDS) was used to identify the material compositions before experiments and conduct post-mortem fractographic analysis. To

explore the strain-rate- and stress-state-dependent mechanical properties, uniaxial compression and indirect tension (Flattened Brazilian disk) experiments under quasi-static and dynamic loading rates were conducted. Digital image correlation (DIC) techniques coupled with high-speed-imaging was performed to obtain full-field strain measurements and investigate surface deformation mechanisms. Lastly, to better analyze the outcomes of this study, mechanical properties and crack speed measurements of the CeramTec Alotec 98% alumina were compared with other ceramics from the literature [1–3, 5, 8, 18, 32–35].

2. Experimental methods

2.1. Material and characterization

The material used in this study was a 98% purity alumina ceramic (CeramTec Alotec 98%) from CeramTec Inc, Germany, where the '98' refers to a nominal composition of Al_2O_3, with the remainder being binding chemicals and impurities. The material was received in a nominal dimension of $100 \times 100 \times 35$ mm^3 thick blocks, and the specimens were machined into cuboids with the dimension of $2.3 \times 2.7 \times 3.5$ mm^3 for uniaxial compression experiments (see Figure 1 (a)), with the loading direction always parallel to the 3.5 mm direction and the imaged surface always being the largest 2.7×3.5 m^2 surface. For indirect tension experiments, the specimens were cut to disks with the size of ϕ8mm $\times$ 4mm, the thickness-to-diameter ratio of 0.5 was used here to obtain a better condition for central crack initiation [36]. In addition, the flatness and parallelism of the specimens were specified to be 0.0005 mm and 0.0025 mm, respectively. To reduce stress concentrations at the flatten edges and facilitate improved loading (i.e., avoid the need for designing arc or strip platens), two parallel flat ends at the disk edge were introduced (see Figure 1 (b)) [4, 25]. This method was also used by Wang et al. [4] where they calculated the tensile strength with various loading angles (i.e., $5°$, $10°$, $15°$, $20°$, and $30°$) according to the Griffith strength criterion [37] using ANSYS software, and they found that only when $2\alpha \geq 20°$ that the crack was most likely to initiate at the centre of the specimen under a uniformly-distributed stress state. This loading angle (i.e., $20°$) was also used in previous studies [18, 25, 26]. For these reasons, $2\alpha = 20°$ was selected in this study for the geometry of our specimen. Figure 1 (c) shows a free body diagram of the indirect tension specimen with loading, P, applied at the flat ends. The loading P, corresponds to the forces generated by the loading platens in quasi-static MTS and the bars in dynamic SHPB experiments (see description later in Sub-section 2.2).

In this study, scanning electron microscopy (SEM, Zeiss Sigma FESEM, 20 kV) equipped with energy-dispersive x-ray spectroscopy (EDS) was performed (AZtec software from Oxford Instrument) to study both microstructure of the as-received alumina and post-mortem fracture surfaces of tested materials, with EDS analysis being used to determine the elemental composition and distribution in the material microstructure. The working distance (WD) was 8.5 mm, and both In-Lens (IL) detector and secondary electron (SE) detector were used to obtain the micrographs of the materials. Additionally, the grain size and crystallographic
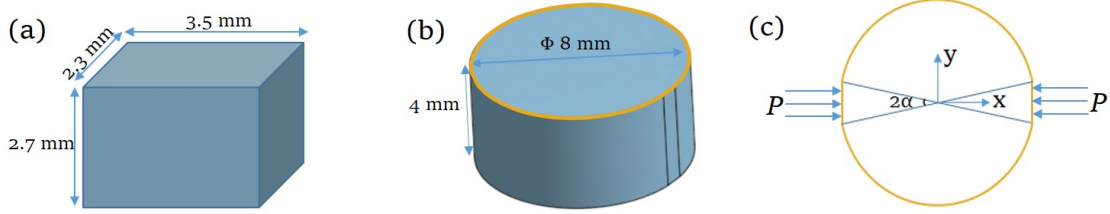
Figure 1: Schematic of dimension and geometry of the specimen used in: (a) uniaxial compression experiments, (b) indirect tension experiments with (c) the top view of (b) with the loading mode and geometries of the sample denoted.

orientation of the grains were studied using EBSD, and the data was post-processed using the AZtec Channel 5 software. Prior to EBSD, the sample was polished with diamond lapping fluids with a minimal grain size less than 0.25 μm to reduce the asperities of the surface. Lastly, the pores and impurities in the as-received alumina were estimated with X-Ray Microscopy (XRM) analysis [13, 38], where scans were performed using a ZEISS Xradia Versa 620 machine with an X-ray voltage of 100 kV at 14.02 W for a total of 1601 projections, with a resolution of 0.5275 per voxel. After scanning, an image processing software (Dragonfly Pro 2.0) was used for 3D reconstruction of the 98% alumina with a central volume of $\phi 4.82$ mm $\times$ 6.66 mm, and image segmentation was performed to extract the porosity and impurity information of the alumina studied here. Together SEM, EBSD, and XRM measurements provide comprehensive information on the microstructural features such as chemical composition, grain shape, size, and internal pore and impurity distribution in the CeramTec Alotec 98% alumina material.

2.2. Mechanical testing set up

Both quasi-static uniaxial compression and indirect tension experiments were performed on a standard MTS series 810 servo-hydraulic machine. A detailed description on this apparatus can be found in a previous study by the authors [12]. In this study, various nominal strain rates of $\sim 10^{-5}$ s^{-1}, $\sim 10^{-4}$ s^{-1}, and $\sim 10^{-3}$ s^{-1} were achieved by using displacement control. The surface deformation process on the sample was visualized and recorded by a high-speed AOS PROMON U750 camera with a full resolution of 1280 $\times$ 1024 pixels. Before testing, speckle patterns were applied using an airbrush with a 0.15 mm diameter nozzle for two-dimensional Digital Image Correlation analysis (2D-DIC). In the quasi-static tests, the framerates were 5, 50, and 500 fps corresponding to the three different nominal strain rates (i.e., 10^{-4}, 10^{-3}, and 10^{-2} s^{-1}), and these framerates were chosen to achieve consistent total frames per experiments for DIC analysis. In this study, the experiments at each strain rate were repeated at least three times at each strain rate to show repeatability.

Dynamic experiments were conducted on a SHPB system, with details on the setup documented previously by Li et al. [12] and Koch et al. [3]. The SHPB system consisted of a projectile, an incident bar, a transmitted bar, and a data acquisition system (HBM Gen 3i at 20 MHz). In the SHPB experiment, the

projectile was launched to hit the incident bar, forming an elastic stress wave that was transferred from the incident bar to the specimen thereby achieving the dynamic loading. In this study, both incident bar (ϕ12.7

130 mm × 304 mm) and transmitted bar (ϕ12.7 mm × 1016 mm) were made of hardened C-350 maraging steel with an elastic modulus of 200 GPa and yield strength of 2.36 GPa. The high stiffness and strength of the bar were designed for testing stiff materials such as ceramics following recommendations from the literature [39]. Two impedance-matched platens made of Ti-6Al-4V titanium alloy jacketed tungsten carbide were attached at two bar-specimen interfaces for protecting the end of the bars from being indented and reducing stress

135 concentration during the loading process. It is worth noting that no protection platens were used in the indirect tension experiments, and this helped with reducing the tendency in obtaining a second peak during unloading (i.e., the increased thickness of the samples may still in contract with the platens upon fracture), and achieving good equilibrium and constant strain rate; no observable indentation on the bar was observed. The sample was placed between two ends of the bar using high pressure grease to minimize frictional effects

140 and reduce lateral force when the sample experienced deformation. The data was collected with two strain gauges (Micro 184 Measurements CEA- 13–250UN-350) attached on the incident and transmitted bar. For the uniaxial compression experiments, the transmitted strain gauge signal, $\varepsilon_t(t)$, was used to calculate the stress-time response $\sigma(t)$:

$$\sigma(t) = \frac{A_0}{A_s} E_0 \epsilon_t(t) \tag{1}$$

where A_0 and A_s are the cross-sectional area of the bar and sample surface, respectively. E_0 is the Young's

145 modulus of the bar.

For indirect tension experiments, the tensile stress is calculated using the load P based on the theory of elasticity [40, 41] through:

$$\sigma(t) = K \frac{2P(t)}{\pi D t} \tag{2}$$

where P is the applied load to the specimen, which is calculated using Eq. (1) without dividing the sample cross-sectional area (A_s). D is the diameter of the specimen, and t is its thickness. K is a dimensionless

150 coefficient that is a function of α (see Figure 1 for specimen schematic), which can be calculated by [4]:

$$K = \frac{cos^3\alpha + cos\alpha + \frac{sin\alpha}{\alpha}}{8(cos\alpha + \frac{sin\alpha}{\alpha})} \frac{\alpha}{sin\alpha} \tag{3}$$

For our case of $2\alpha = 20°$, K is calculated to be approximately 0.95 by Eq. (3) [4].

The measurement signals were acquired using an HBM Gen3i High-Speed Recorder sampling at 20 MHz with a Bessel IIR pre-filter to eliminate low frequency noise. A Shimadzu HPV X-2 ultra-high-speed camera with a full resolution of 400 × 250 pixels was used to capture the surface deformation process and obtain

155 images for post-DIC analysis. In the dynamic experiments, with the current selection of subset and step sizes,

6

the overall confidence intervals for correlation from the VIC 2D software is consistently within the range of 10^{-3} to 10^{-4} pixels (i.e., ~ 30 pixels/mm for indirect tension experiments and ~ 69 pixels/mm for compression experiments). The DIC measurements are verified by comparing against train gage measurements, and baselining against Al 6061 and round robin testing [31] The camera frame rate (i.e., from 0.5 to 2 million frames per second) and exposure time (i.e., from 200 to 500 ns) were adjusted based on the loading rate, and a total of 128 frames were obtained for each experiment. For the uniaxial compression experiment, a K2 DistaMax Infinity lens was used to fill the whole specimen into the field of view, and a SIGMA F2.8EX DG MACRO OS lense was used for the larger indirect tension specimen.

In both quasi-static and dynamic experiments, the uniform surface deformation was checked by taking areas of interest (AOI) across the whole specimen surface (see Figure 4 and Figure 5) using the VIC-2D V6 software, and the average value of the full-field data was taken for further analysis. The strain information was combined with the engineering stress (Eq. (1) for compression or Eq. (2) for tension) to generate stress-strain curves. In DIC analysis, the first image of each test was selected as the reference (undeformed) image. The subset size was chosen as ~ 50 pixels for quasi-static experiments, with a step size of ~ 5 pixels judging by the smoothness of the strain curves. In the dynamic experiments, the subset size was chosen as ~ 25 pixels with a step size of 1 pixel to increase the accuracy of the measurement. During analysis, the zero-normalized square sum of difference (ZNSSD) method was chosen to perform the correlation [42]. A Gaussian low pass filter was selected to filter out the undesired high frequency signals and pre-smooth both reference and deformed images, and this improved the accuracy of the output curves [43]. The "Optimized 8-tap" interpolation scheme was selected for the highest order of the spline scheme.

In the dynamic experiments, pulse shaping techniques were used to obtain a linear ramp loading profile desired for the brittle solids [18, 20], and these shaping techniques ensured stress equilibrium and constant strain rates. Specifically, in uniaxial compression experiments, strain rates between ~ 70 to 120 s^{-1} were achieved by using tin pulse shapers ($\phi 4$ mm and 1.58 mm), strain rates between ~ 350 to 840 s^{-1} were reached with HDPE pulse shapers ($\phi 4$ mm and 1.58 mm) with different projectile length (300 mm and 126 mm), and strain rates between ~ 730 to 1200 s^{-1} were achieved using paper pulse shapers with a 300 mm projectile length. The primary goal of the paper pulse shaper was to reduce the background noise and dispersion during loading [21, 44]. For indirect tension experiments, strain rates between ~ 10 to 20 s^{-1} were achieved with tin pulse shapers, strain rates between ~ 25 to 40 s^{-1} were reached with HDPE pulse shapers, and strain rates between ~ 90 to 170 s^{-1} were achieved with paper pulse shapers using similar project lengths as the compression tests. It is observed that at the same pulse shaping condition, the strain rate achieved in the indirect tension experiments were almost an order lower than that in the uniaxial compression experiments, and this was consistent with the literature [18]. The one order lower in strain rates for the indirect tension experiments was a consequence of specimen sizes, which were limited by: 1. enabling failure under accessible

forces from the gas gun, 2. compensating for bar size, and 3. enabling sufficient spatial resolution during high-speed imaging for better surface deformation visualization and DIC analysis. Additionally, checking the experimental validity for both uniaxial compression and indirect tension experiments is of importance to ensure that the true mechanical response of the material is captured, and this also constitutes one of the focuses in this study (see later in Sub-section 3.2 for details). After both the quasi-static and dynamic SHPB experiments, alumina fragments were collected for post-mortem microscopic analysis to further investigate the fracture mechanisms.

3. Results and discussion

This section presents characterization and stress-state- and strain-rate-dependent mechanical testing results of the CeramTec Alotec 98% alumina ceramic. Specifically, Sub-section 3.1 details the SEM-EDS and XRM results showing the microstructural features of the material. Sub-section 3.2 shows the validity of SHPB experiments which is demonstrated with DIC analysis. Following this section, we will show time-evolved stress, strain, and failure evolution in uniaxial compression and indirect tension experiments in Sub-section 3.3. After that, stress-state- and strain-rate-dependent stress-strain responses are demonstrated and discussed in detail in Sub-section 3.4. Crack speed measurements are conducted to provide insights into the differences of crack propagation in the material under tension dominated and compression dominated stress states in Sub-section 3.5. Lastly, damage evolution and fracture analysis that are carried out to investigate the failure modes of the material are presented in Sub-section 3.6.

3.1. Material characterization with SEM-EDS and XRM scanning

Figure 2 is an SEM micrograph with the corresponding EDS maps showing microstructural features and elemental information. Note that the surface pores observed in the SEM micrograph may be generated from the sample preparation process (i.e., polishing), and therefore, it is not a representation of the porosity and pore size of the material. Instead, the porosity analysis has been conducted using only the XRM data (see later in Figure 3 (b)). EDS maps on the right column of Figure 2 shows the elemental composition and distribution of the current alumina, with the brighter areas corresponding to higher concentrations of the noted element. The EDS maps show that the oxygen and aluminum are present everywhere, confirming the major constituent of the material (i.e., Al_2O_3), while spots (i.e., silicon, calcium, magnesium, and carbon) are weakly scattered around the spots. Silicon, calcium and magnesium are believed to come from manufacturing process [3], and the carbon is most likely caused by environment contamination and sample preparation where carbon powder is entrapped within the deep spots during carbon coating process.

Figure 3 (a) shows the histogram distribution and cumulative distribution function of the equivalent circle diameter with an inserted EBSD inverse pole figure (IPF) taken on the as-received alumina surface.
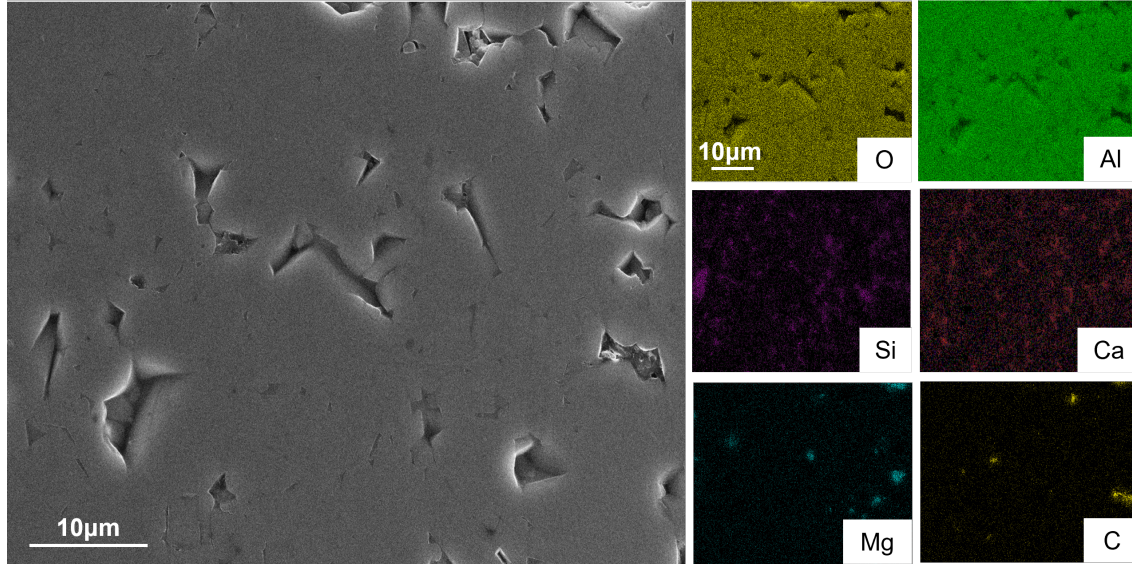
Figure 2: SEM micrograph with corresponding EDS maps and analysis of the as-received CeramTec Alotec 98% alumina showing pores and impurities. The EDS elemental maps indicate trace amounts of Si, Ca, and Mg. Note that C is from contamination and sample preparation, and the location and size of impurities can be related to unindexed regions in the EBSD map later in the Figure 3.

The average grain size of the current alumina is computed as $\sim 1.85 \pm 0.98$ μm, which is smaller than the grain sizes reported in the literature for other commercially available alumina (e.g., ~ 3.9 μm [32], ~ 4 μm [33], ~ 25 μm [6]). Specifically, the large standard deviation in our alumina material is associated with the bi-model distribution in the grain size. From the IPF map, in Figure 3 (a), the material microstructure consists of large amounts of nearly circular small grains (ranging from 0 to 2 μm) randomly distributed in the whole area of map and encompassed with relatively small number of large horizontal high-aspect-ratio grains (ranging from 6 to 8 μm). Next, both small equiaxed and large columnar grains appear to have no preferred crystal orientation and most boundaries are of high misorientation angle ($>15°$). Lastly, unindexed areas in the IPF map with irregular shape are observed, and they are believed to be corresponding to either the pores or regions with impurities in the EDS maps (see Figure 2). Overall, the grain structure of the current alumina material is different from the ones observed in the previous studies (i.e., higher aspect-ratio grain, grain size [45, 46]), and some potential reasons are: 1. the high-aspect-ratio grain structure can be related to the presence of Ca (content of Ca is indicated in EDS maps). In previous work by Dillon et al. [47], Ca-doping was observed to effectively alter the grain morphology towards high aspect ratio (i.e., grain elongation), and this was attributed to the disordered grain boundary resulting from CaO segregation; and 2. temperature and pressure gradients during fabrication have also been associated with the nonuniform microstructure [48], although this is challenging to verify.

Figure 3 (b) shows the histogram distribution of the relative frequency of the volume of pores and

9

²⁴⁰ impurities of the current alumina material extracted from the XRM scan reconstruction. An inserted sub-figure shows a 3D rendering of the reconstructed XRM scanned volume with pores and impurities color coded, as well as 2D images on the right showing the representative thresholding of the X-Ray Microscopy Analysis performed using Dragonfly Pro 2.0. It is observed that the pores and impurities are evenly distributed throughout the material, with some local amalgamations existing in the scanned volume, and this explains

²⁴⁵ the large unindexed areas observed in the IPF map (see previously in Figure 3 (a)). The total volume of the pore and impurity population in this sample was determined to be less than 1.3% with Dragonfly Pro 2.0 software, which is a common value in dense alumina [49]. From the histogram of the pores and impurities volume, almost all of them are concentrated at volumes less than 1.4 μm^3 (note that the second bar in the volume histogram is nearly ten to the power of four lower than the first bar). Overall, the pores and

²⁵⁰ impurities can act as the stress concentration sites or "weak spots" in the strong and hard alumina matrix, facilitating crack initiation and growth [49], which will, in turn, affect the mechanical performance of the material.
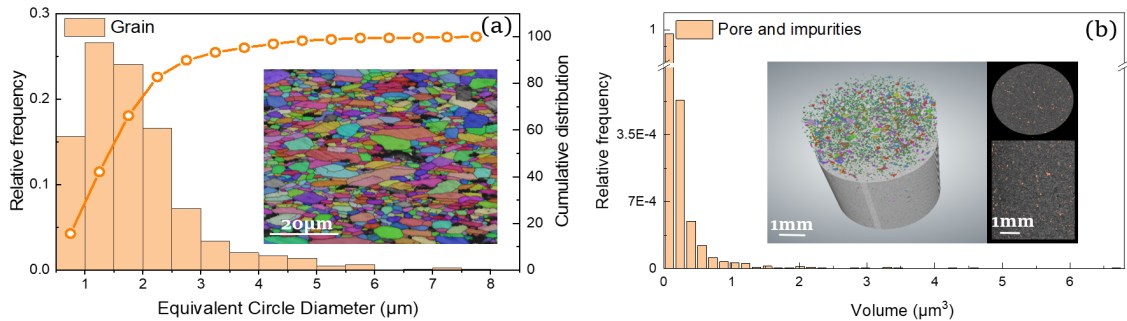
Figure 3: (a): Histogram distribution of the equivalent circle diameter showing bi-modal grain size distribution of the CeramTec Alotec 98% alumina. The inserted figure is an EBSD inverse pole figure (IPF) taken on the as-received alumina surface showing grain morphology. The dark regions in the IPF map correspond to the unindexed areas, indicating locations of pores and impurities. (b): Histogram distribution showing relative frequency of pores and impurities acquired using X-Ray Microscopy. The inserted figure is a 3D render of the reconstructed X-Ray Microscopy scanned volume with pores and impurities color coded. The 2D images on the right show the thresholding of the X-Ray Microscopy Analysis.

3.2. Validity of SHPB experiments through DIC analysis

Prior to presenting the rate-dependent mechanical property measurements, the validity of the SHPB

²⁵⁵ tests is demonstrated in this sub-section. Shown in Figure 4 is a compressive stress vs. time curve and strain vs. time (left figure) extracted from both the global and local area of interests (AOIs) from the DIC software (right figure). The strain rate of this experiment is ~ 444 s^{-1} and the imaging framerate is 1 Mfps, which belongs to the corresponding stress-strain curve shown later in Figure 8. Compressive loading is in the horizontal direction in the image. While all considerations mentioned here are analogous to classical

²⁶⁰ (strain gage) approaches to check equilibrium in the absence of imaging information, it is also a part of

the authors' methods to check for good equilibrium by checking for force balance across the sample (not shown for brevity here). From Figure 4, it is found that strain curves during compression experiments from all AOIs overlap with each other closely and present a linear increasing trend starting at around 18 μs, indicating mostly uniform deformation (i.e., from the overlapping for strain-time curves) and constant strain rate (i.e., from the near-constant slope of the strain-time curves) are achieved during the SHPB compression experiments. It is also observed that strain-time curves follow well with the stress-time curves, demonstrating good equilibrium has been reached, and therefore, a linear elastic stress-strain curve can be obtained (see later in Figure 8 for matched curves). Similar approaches have been used in previously studies to demonstrate the validity of compression experiments [3].
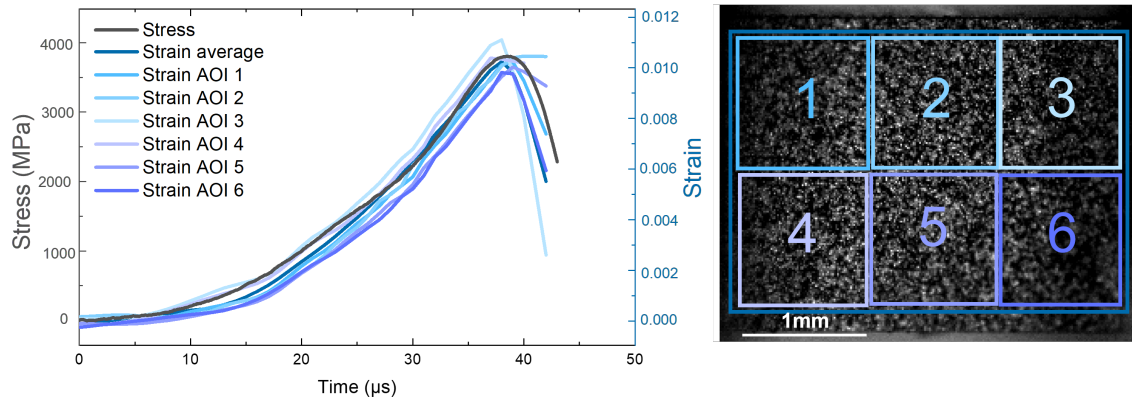
Figure 4: (Left) Compressive stress and strain curves as a function of time of different AOIs for alumina and (right) the sample showing the various location of the DIC AOIs. The loading direction is horizontal in the right image. The average strain vs. time curves overlap with each other, indicating uniform deformation and good equilibrium. The strain vs. time curves trace the stress vs. time curve well, indicating a linear elastic behavior of the material. The slope of the strain-time is reasonably linear, indicating a constant strain rate of 444 s^{-1}.

Next, to demonstrate the validity of the indirect tension experiments, Figure 5 shows the typical displacement curves of the upper and lower half of an indirect tensile sample plotted against time in an SHPB experiment (left), with the corresponding DIC contours at four different times (right). The contours are associated with the time points a-d marked on the displacement curves (right, top). The strain rate of this experiment is $\sim$ 444 s^{-1} and the imaging framerate is 1 Mfps. To better visualize the surface deformation, a series of high-speed still images with the contour removed are shown in the second row (right, bottom). The material is diametrically loaded in the horizontal direction in the still images, then the fracture starts internally. In Figure 5, the displacement curves of the upper and lower half of the sample show an initial gradual rise with time followed by a quick increase near the point d (marked in the average curve), where point d corresponds to the rapid propagation of the surface axial crack at the center of the specimen (see (d1) and (d2)). A reasonable symmetry is observed between the upper and lower halves of the specimen

11

which results in the cancellation of each other when the average is computed (~ 0) (see Figure 5 (a1)-(d1)). It is observed that no obvious deformation is found in (a1) and (b1) with the vertical displacement (v) at ~ 0 (green color in the color bar). The contour color changes to a higher level in image (c1) and then forms two distinct semicircle parts with a boundary line in the diametrical loading direction in image (d1). In (c1), the left part of the bottom semicircle experiences small compression strains and the right part experiences slightly positive tension strains. This is a consequence of the crack initiating from the middle and propagating outward. The displacements observed to be 'red' (v ~ 0.02mm) in the upper half and 'purple' (v ~ 0.02mm) in the lower half are demonstrative of a near-symmetric tensile mode failure of the sample and good equilbrium, as is desired in Brazilian disk experiments [1]. The high-speed still images on the right in Figure 5 show the incubation (see (b2)), initiation (see (c2)), and propagation (see (d2)) process of an axial splitting crack. Taken together, these results support the validity of the Brazilian disk experiments [35].
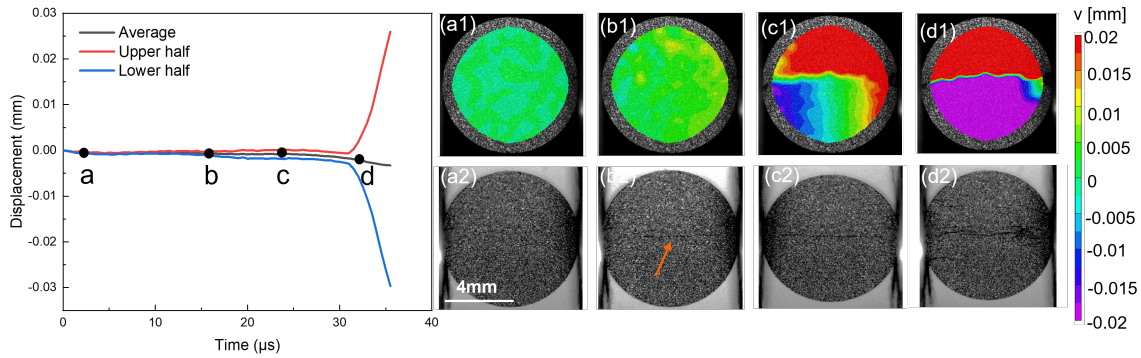
Figure 5: Plot of displacement of upper and lower half of alumina indirect tension sample vs. time during a dynamic experiment at a strain rate of 109 s^{-1}, (a1)-(d1): DIC contour corresponding to the time a-d marked on the displacement curves. The symmetric displacement curves and DIC contour indicate good stress equilibrium and failure during the loading process. (a2)-(d2): Images showing the crack growth process, with an opening crack initiating in the middle of the specimen in image (b2) (marked with an orange arrow), propagating in image (c2), and spanning the surface in image (d2). The loading is horizontal in the image.

3.3. Time-evolved stress, strain, and failure evolution in uniaxial compression and indirect tension experiments

Shown in Figure 6 is the compressive stress and strain history curves coupled with ultra-high-speed camera images showing the time-evolved failure. The high-speed still frames on the right are covered by DIC contours to better demonstrate the axial strain (ε_{xx}) evolution associated with the onset of fracture, taken from a dynamic compression experiment. The image frame letters (a-f) correspond to those labelled on the stress-time curve on the left. In this experiment, the strain rate is ~ 625 s^{-1} and the imaging framerate is 1 Mfps, with the strain rate being estimated by the slope of the strain-time history (see the red dashed line). The peak strength is 4287 MPa, and this occurs at ~ 40 μs in 2 frames before the first crack appears on

12

the imaged surface. The corresponding axial ($\varepsilon_{\mathrm{xx}}$) and lateral ($\varepsilon_{\mathrm{yy}}$) strains at peak strength are ~ 0.014 and ~ 0.0035, respectively, and this gives an instantaneous Poisson's ratio of 0.25. Note here that the evolution of Poisson's ratio will be further studied by taking the ratio of the lateral and axial strain-time curves later in Figure 11. It is worth noting that the shear strain ($\varepsilon_{\mathrm{xy}}$) curve is almost zero throughout the experiment, indicating no in-plane rotation occurs during the loading process and an indicator of a good uniaxial compression experiment. For the images on the right, frame (a) is taken at the beginning of the test with zero strain for reference. The purple contour indicates zero axial strains (see the color bar). Frame (b) is taken during loading at two frames before the peak stress is reached, with the contour showing a near-homogeneous distribution of the strain on the specimen surface during loading. At this moment, there is no visible crack observed on the specimen surface (i.e., no strain localization). Frame (c) is taken at the first frame where axial cracking starts to appear on the specimen surface. It is observed that some cracks have been initiated at the bottom of the specimen causing the loss of DIC correlation. In addition, strain concentrations are observed at the top of the specimen (red areas shown in contour of frame (c)), which indicates another site for fracture nucleation. In frame (d), about 3 μs after peak strength, an axial crack spanning the specimen is observed at the strain localization zone in frame (c), and a new strain concentration site is observed in the middle of the specimen causing the appearance of another primary axial crack (see orange arrows). In frame (e), multiple cracks grow accross the specimen, and this leads to continuous degradation in load carrying capacity as shown in the stress-time curve (left in Figure 6). Lastly, frame (f) shows the near-end state before the catastrophic failure of the specimen. Note that DIC maps could not be obtained with excessive strain discontinuity after this time/frame. It is observed that the peak strength sustained (right before frame (c)) is attained well before the crack coalescence occurs (in frame (d)), indicating that structural-scale cracking is a significant factor that influences the property of the materials. Later, we will also use measurements of the growth of the first few primary cracks to inform on how the crack speeds are different between the compression and indirect tension cases (see later in Figure 12).

Next, shown in Figure 7 is the indirect tension stress and strain history curves coupled with ultra-high-speed camera images depicting time-evolved failure of the material in a tensile stress state. The $\varepsilon_{\mathrm{yy}}$ contours are overlaid on the time-resolved images on the right in order to show the initial crack evolution and fracture process. The strain rate in this experiment is $\sim 27\ s^{-1}$ and the imaging framerate is 0.5 Mfps, with the peak stress being 344.3 MPa calculated by Eq. (2) when the maximum load P_{max}, is achieved. From the strain vs. time curves shown in Figure 7, near-linear increase in $\varepsilon_{\mathrm{xx}}$ and $\varepsilon_{\mathrm{yy}}$ strains are observed with strains at peak stress reaching ~ 0.002 and ~ 0.0011, respectively. The shear strain ($\varepsilon_{\mathrm{xy}}$) is near zero, confirming negligible in-plane rotation in the sample during loading and a reasonable accuracy for measuring peak strength. The near-zero shear strain achieved in this study using t/D = 0.5 represents improvements over previous works [24], and therefore, provides a more consistent data set for assessing material mechanical response in
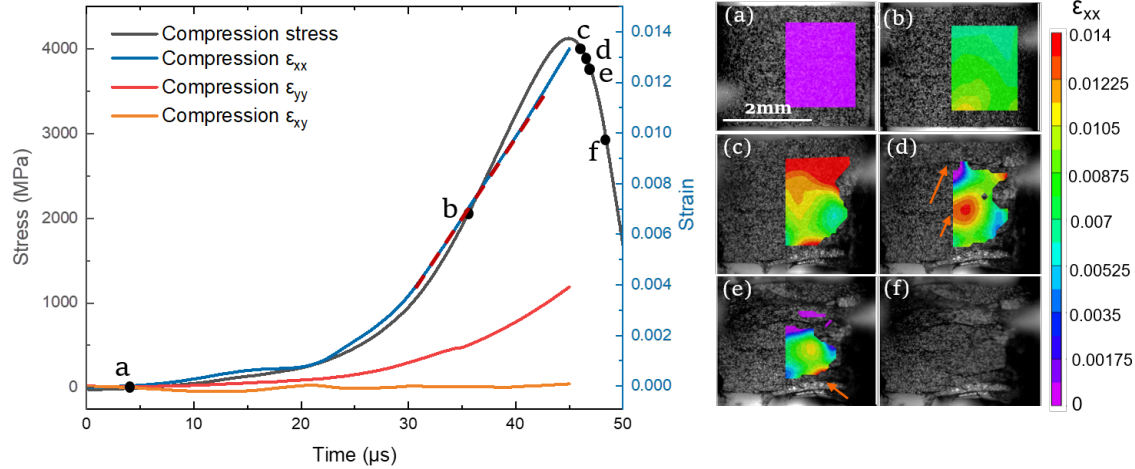
Figure 6: Compressive stress and strain curves as a function of time obtained at a strain rate of 624.5 s^{-1} coupled with ultra-high-speed camera images showing time-evolved failure. (a)-(f) images with ε_{xx} contours showing cracking initiates in image (c), and grows and spans the surface in (d)-(e) until ultimate failure in (f). Image (c) and (e) are taken right before and after image (d), demonstrating images used later when performing crack speed measurements for the primary crack.

335   tension. Shown on the right side of Figure 7 is a sequence of high-speed still frames demonstrating real-time visualization of the loading event, half covered by DIC contours showing the lateral strain (ε_{yy}) evolution associated with the onset of fracture. The image frame letters (a) to (f) correspond to those labelled on the stress-time curve. By consistently taking the whole specimen surface as the AOI, average strains for ε_{xx}, ε_{yy}, and ε_{xy} are computed by averaging over the top or bottom hemisphere of the disk up to the point where the

340   primary crack initiation starts (see frame (c)). After this point, the crack continues to grow and open (see frame (d) and (e)), and the correlation is lost eventually (see frame (f)). Frame (a) and (b) show the sample surface before the first axial crack appears, where the strain distribution is near-uniform across the specimen surface. In frame (c), the ε_{yy} strain localizes at the center of the sample (see the red arrow), suggesting the location of crack initiation. This is important because it aids in justifying the validity of the experiment

345   by confirming fracture initiation in near the middle of the specimen with a lateral cracking opening mode [2, 4]. When the load raises further, in frame (d) right after the peak stress, an initiation of an axial crack from the previous strain concentration region at the center of the specimen is observed, and the propagation of the crack can be traced by the growth of the red contour zone from (c) to (d). Frame (e) shows the further growth of the crack to the edge of the specimen, splitting the sample into two semi-circle pieces

350   axially, and this results in rapid unloading. In frame (f), more primary cracks propagate across the sample diametrically and secondary cracks at the edge of the sample close to the primary cracks are generated, resulting in catastrophic failure. This primary axial splitting followed by secondary circumferential crack growth and the resulting fracture pattern has been observed in other experimental and numerical studies on different ceramic materials [21, 28], and this is considered a favorable fracture pattern indicating the validity

14

of an indirect tension experiment [4]. Later, we present measurements of these crack speeds.
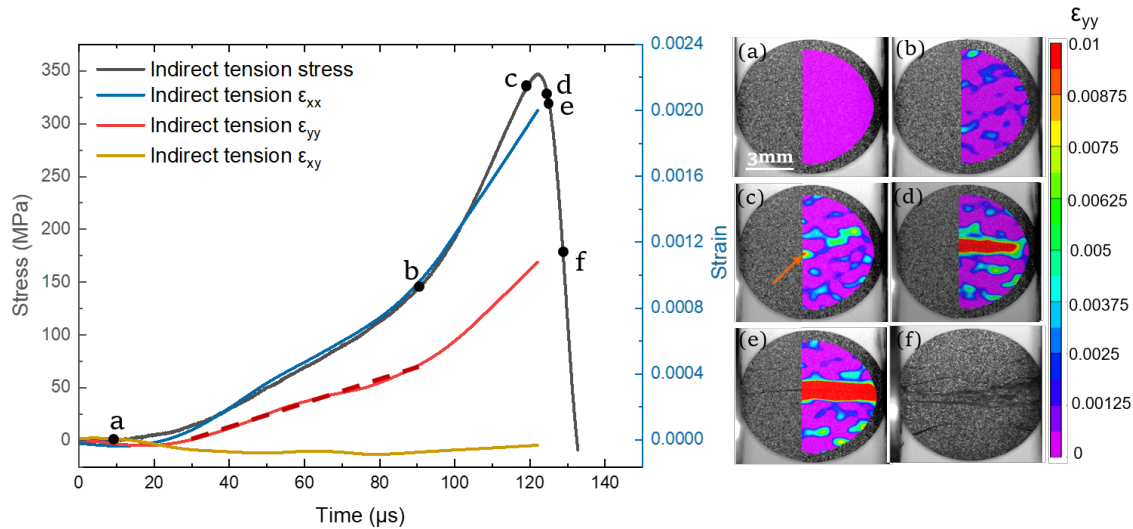
Figure 7: Indirect tension stress and strain history curves performed at a strain rate of 27 s^{-1} with ultra-high-speed images and overlaid ε_{yy} contour. Strain vs. time curves show near-linear increasing ε_{xx} and ε_{yy} strains with near zero ε_{xy} strains, indicating a good experiment. The ε_{yy} strain localizes at the center of the sample (see image (c)), and this is believed to be the location of crack initiation.

3.4. Stress-state- and strain-rate-dependent stress-strain response

Shown in Figure 8 are the representative stress-strain curves (darker color indicates higher strain rate, with values noted in the corresponding legends) of thirty-three (33) uniaxial compression experiments with the strain rate ranging from 2.0×10^{-4} to 1024 s^{-1} (including eight (8) in quasi-static and twenty-five (25) in dynamic loading) and twenty-one (21) indirect tension experiments ranging from 2.7×10^{-6} to 174 s^{-1} (including four (4) in quasi-static and seventeen (17) in dynamic loading). From Figure 8, for both stress states, it is found that the stress increases mostly linearly up to the peak stress, indicating an elastic behavior before failure, as is expected for brittle materials. In this study, the slope of the stress-strain curve is defined to be the Young's modulus of the material. For the quasi-static experiments, the average Young's modulus is 332 ± 25 GPa for the uniaxial compression experiments and 342 ± 16 GPa for the indirect tension experiments. For the dynamic experiments, the average Young's modulus is 368 ± 39 GPa for the uniaxial compression experiments and 376 ± 27 GPa for the indirect tension experiments. Given a slightly larger variation in measurements from the dynamic experiments, the measured elastic modulus are in good agreements with the reported values of ∼ 370 GPa in both industrial datasheets [50] and previous studies for alumina [51]. In addition, the elastic modulus show no stress-state- and strain-rate-dependencies, which is expected and assumed in other studies [16]. Finally, it is also observed that when the achieved failure strain under both a compressive (e.g., ∼ 0.01) and indirect tensile (e.g., ∼ 0.01) stress state is reached, the

15

tensile peak strength of the material is almost an order of magnitude lower than that under the compression. In addition, dynamic tests generally show higher failure stress than quasi-static tests, with the strain-rate-dependent strength measurements further demonstrated in Figure 9.
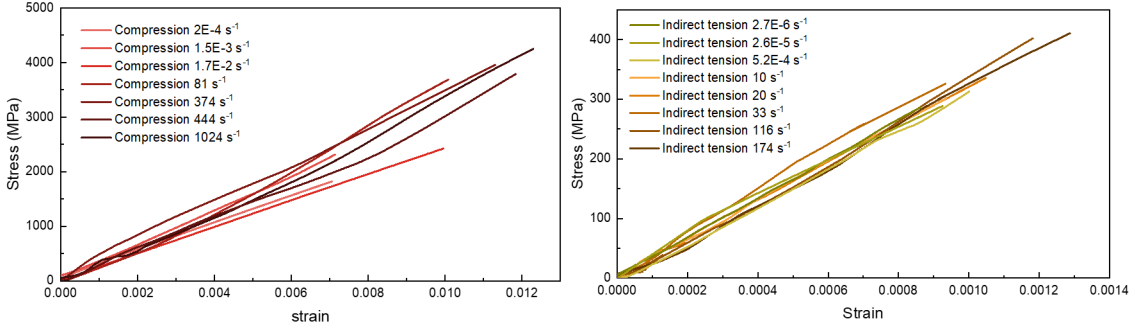
Figure 8: Representative stress-strain curves of CeramTec Alotec 98% alumina for uniaxial compression (left) and indirect tension (right) experiments across all strain rates in this study (between 2.0×10^{-4} and 1024 s^{-1} for uniaxial compression and between 2.7×10^{-6} and 174 s^{-1} for indirect tension). The curves are mostly linear and the dynamic tests show higher failure stress than quasi-static tests, as would be expected. For the quasi-static experiments, the average Young's modulus is 332 ± 25 GPa for the uniaxial compression experiments and 342 ± 16 GPa for the indirect tension tests. For the dynamic tests, the average Young's modulus is 368 ± 39 GPa for the uniaxial compression experiments and 376 ± 27 GPa for the indirect tension experiments.

Next, Figure 9 (a) shows the peak strength plotted against the log scale of the strain rate for both indirect tension and uniaxial compression experiments. Figure 9 (b) and (c) are enlarged images of the regions marked with red squares in (a). From Figure 9 (a), it is observed that the peak strength of the indirect tension experiments is around 10× smaller than the peak strength from the uniaxial compression experiments. For the quasi-static experiments, the peak strength varies from 2467 to 3916 MPa across the range of 1.7×10^{-5} to 1.7×10^{-3} s^{-1} for uniaxial compression experiments, and from 282 to 320 MPa across the range of 2.7×10^{-6} to 5.2×10^{-4} s^{-1} for the indirect tension experiments. For the dynamic experiments, the peak strength varies from 3290 to 5411 MPa across the range of 71 to 1227 s^{-1} for uniaxial compression experiments, and from 339 to 422 MPa across the range of 10 to 178 s^{-1} for the indirect tension experiments. Overall, the peak strength shows a strain-rate-dependency in both cases and is more pronounced under dynamic loading.

To compare the strain-rate-sensitivity in uniaxial compression and indirect tension, a linear fit on peak strength in the form of $\sigma = a\dot{\varepsilon}+b$ is applied to all dynamic uniaxial compression experiments (see Figure 9 (b)) and dynamic indirect tension experiments (see Figure 9 (c)) , where σ is the peak strength and $\dot{\varepsilon}$ is the strain rate. Here, a and b are fitted coefficients. A higher slope value (i.e., the value of a) in the compression tests (~ 0.68) than tensile tests (~ 0.39) is observed, indicating a greater strain-rate-sensitivity on the compression peak strength than tensile peak strength. In addition, the variability of the strength is indicated with R^2 values of 0.26 for compression experiments and of 0.70 for tensile experiments in reference to the quality of
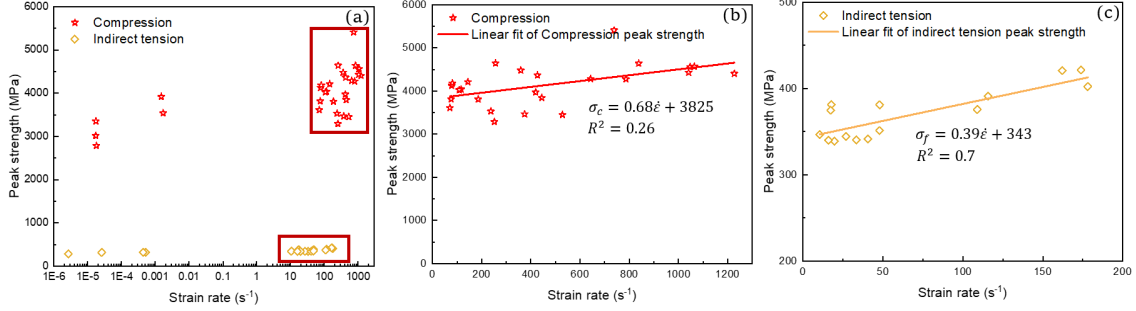
Figure 9: Summary of the strain-rate dependent peak strength of the CeramTec Alotec 98% alumina for both indirect tension and uniaxial compression experiments. Figure b and c are enlarged images of the regions marked with red squares. A linear fit on peak strength in the form of $\sigma = a\dot{\epsilon} + b$ is used to compare the strain-rate-dependency of the two stress states, which is discussed in the main body.

the linear fit. Material variability (e.g, grain sizes) and experimental uncertainties are potential reasons for the variation in strengths (i.e., a lower R^2 value indicates a higher variability in strength with respect to strain rate) [52]. In previous studies, power-law fits with different exponents have been used extensively to trace the strain-rate-dependency of the strength for brittle solids [7, 53]. For example, Lankford et al. [6] used a power law fit with an exponent of 1/3 to represent the rate-dependency of strength and the model captured the low- and high-rate of the strength response. In another study, a scaling law by Kimberley et al. [53] was used with a 2/3 power of the strain rate at high strain rates. Here, the strain-rate-dependency of the materials has been attributed to initiation, growth, and interactions of cracks [53], with many previous studies showing rate-dependency in a number of ceramics [18, 54, 55]. In this study, instead, linear fits are used only within the dynamic regime because: 1. given the tighter range of strain rates that can be achieved in the dynamic regime using the SHPB technique (i.e., usually within an order between 10^2 and 10^3 s^{-1}), it prevents lumping all the data points into a small region on the semi-log plot; 2. it demonstrates the scattering in strength better with the R^2 value, which is usually expected given the material variability and complex structural damage evolution; and 3. it does not diminish the purpose of showing the strain-rate-dependency since the quasi-static strength is often taken as the "reference" strength of the material, and according to the power laws, the transient strain rates are mostly neglected and assumed to be the same strength as the quasi-static one [56].

Lastly, a summarized plot of compressive and tensile peak strengths vs. strain rate of different ceramics (mostly alumina) is shown in Figure 10. The plot includes other alumina ceramic materials (i.e., AD995 [3, 5, 8, 32, 34], AD85 [3, 8], AD94 [8], AD98 [2, 8], JSI [32], MTU [33], Cervar [33], Lucalax [33]) and other ceramic materials (i.e., glass-ceramic [15], TiB$_2$-B$_4$C [18], and ZrB$_2$-20%SiC [35]). We include non-alumina ceramics for the indirect tension experiments because of the limited data in the literature on alumina for tensile stress-states. From Figure 10, it is found that the current CeramTec Alotec 98% alumina shows

17

higher compressive strength than most other alumina (e.g., Cervar, Lucalax, AD995 and AD85). The smaller average grain size ($\sim 1.85\ \mu$m) relative to other ceramics is likely a factor contributing to the relatively higher strength [49]. For indirect tension data, the studied alumina has a relatively higher tensile strength than AD94 [8], AD995 [8], and AD98 [2] alumina at the same strain rates. Differences in strength are related to grain size [46] and porosity [50] effects. Comparing with other brittle materials, the CeramTec Alotec 98% alumina has a comparable tensile strength with that of the TiB$_2$-B$_4$C ceramic, while the strength of the studied alumina is $\sim 12\times$ higher than the glass-ceramic [15] at quasi-static loading and $\sim 8\times$ higher at dynamic loading. Overall, results show $\sim 10\times$ to $14\times$ greater of compressive strength than tensile strength.
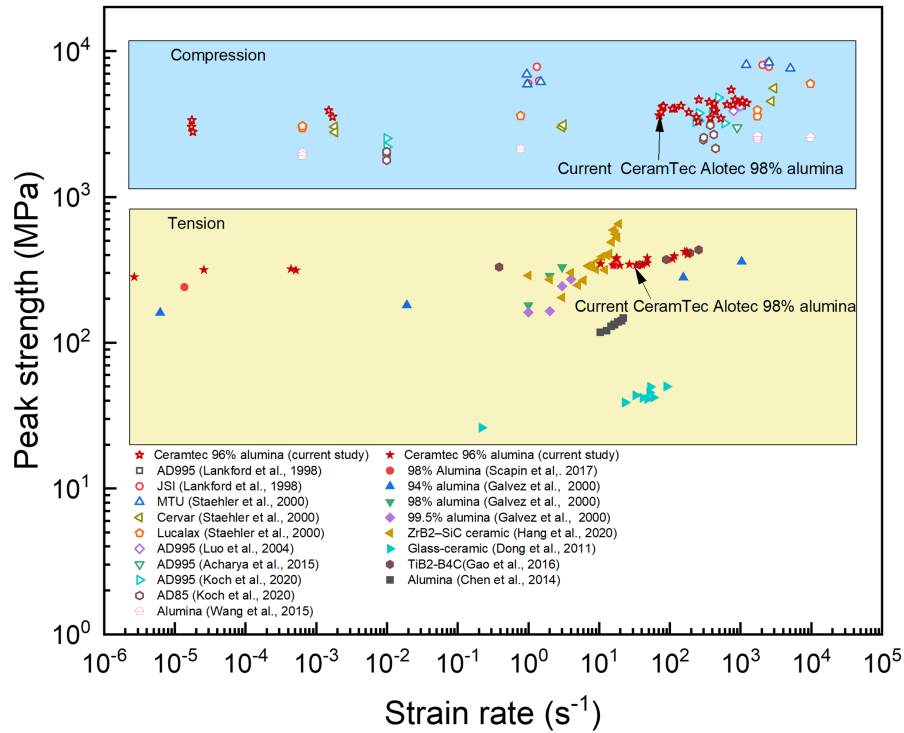
Figure 10: Log-log plot of the uniaxial compression and indirect tensile strength of the studied alumina against strain rate together with the data of different ceramic materials in previous literature [1–3, 5, 8, 16, 18, 32–35].

3.5. Poisson's ratio evolution and crack speed measurements

In this sub-section, damage evolution is explored in terms of Poisson's ratio evolution (see Figure 11) and crack speed measurements (see Figure 12). First, the lateral strain vs. axial strain history for uniaxial compression at strain rates ranging from 71 to 1227 s^{-1} and indirect tension experiments at strain rates ranging from 11 to 174 s^{-1} are shown in Figure 11. The curves for quasi-static loading are not plotted because the post-peak stress failure process is not captured due to limitations in the camera frame rate. The average Poisson's ratio is 0.237 ± 0.02 for the uniaxial compression experiments, and 0.240 ± 0.03 for the

18

indirect tension experiments. These are obtained by taking the slope of the lateral vs. axial strain plot up to the failure point (peak in the stress-time curves in Figure 6 and Figure 7, and turning point in the lateral vs. axial strain curves here). The calculated Poisson's ratio value agrees well with the values reported in previous studies on alumina [1, 7, 27] (i.e., ~ 0.23), further verifying the accuracy of the DIC measurements.

435 In both cases, the Poisson's ratio remains constant until failure, where the differences occur in the collapse part of the curves. It is observed that in the uniaxial compression experiments, the collapse curves generally shoot backwards, while the collapsed curves for indirect tension generally shoot more upwards indicating more rapid failure, which is attributed to the more unstable structural failure under the tensile stress state [3]. It is worth noting that unraveling effects of, for example, strain rate is challenging in this data set given

440 the interplay between fracture initiation, growth, and coalescence behaviors. More advanced techniques, such as microscopic mechanical testing with in situ measurements and imaging are needed to investigate the coupling of damage evolution depending on stress states and strain rates [57].
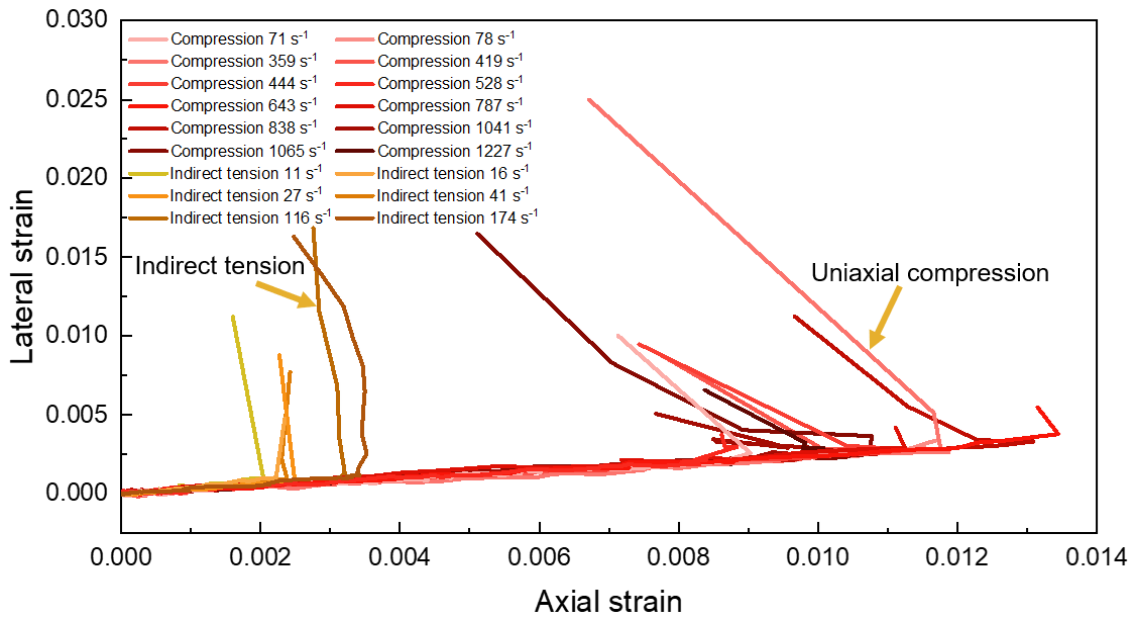
Figure 11: Lateral strain vs. axial strain plot for indirect tension and uniaxial compression experiments under dynamic loading. The average Poisson's ratio is 0.237 ± 0.02 for the uniaxial compression experiments, and 0.240 ± 0.03 for the indirect tension experiments. The difference between two stress states is observed at the end of the curves (i.e., stress collapse), where the material is undergoing failure.

Next, shown in Figure 12 is the crack propagation speed estimated in both indirect tension and uniaxial compression experiments and plotted against strain rate. Corresponding ultra-high-speed images showing

445 the schematic definitions of primary and secondary cracking are also included (right figures). For indirect tension experiments, the primary crack speed is defined as the velocities of the first crack that initiates and propagates from the center of the specimen (frame (a) to frame (b), marked with a red star in subset image),

and the secondary crack speed is defined as the cracks that appear next in time and in the circumference of the primary crack (frame (c) to frame (d), marked with a green star), with the location mostly originating from the edge of the sample. The length of the secondary crack is shorter than the primary crack and limited within half of the diameter of the Brazilian disk, indicating that the failure is dominated by the tensile stress field in the middle of the sample. For the uniaxial compression test, the primary crack speed is defined as the velocities of the first three major cracks that appear and span the sample surface during testing (frame (e) to frame (f), marked with a orange diamond). Note that the secondary crack speed in uniaxial compression was not counted because the crack density is too great at this time and the portion of the specimen will be outside the depth of view. No quasi-static experiments are plotted because the camera in this case is not fast enough to record crack velocities. For both indirect tension and compression experiments, the crack speeds are determined by tracking the crack tip displacements of the growing cracks over a number of frames (shown with arrows in the sub-images). The crack speed is determined by time averaging over these frames, with similar methods being used previously by Kannan et al. [58]. Specifically, in the indirect tension experiments, the displacement of the primary crack is tracked over 2 to 20 frames (depending on spanwise propagation) and then averaged over those frames to determine a crack speed measurement. For compression experiments, after finding the three major axial cracks that span the entire specimen surface, similar measurements are performed for each crack over 2 to 6 frames and then averaged across those times to determine the crack speed values. Three primary crack speeds for compression tests, and one primary crack speed and one secondary crack for the indirect tension tests are included in Figure 12. The deviation in measurements is associated with changes in velocity across consecutive frames, as well as some uncertainty in the location of the crack tip across these frames. Uncertainties in measurements may also come from the manual identification of the length of the cracks and selection of frames (adjacent frames with similar crack length). Therefore, we use ultra-high-speed camera frame rates ranging from 1 to 5 million and measure different sets of points along the crack front for an average speed value for each single crack to reduce error. From Figure 12, the primary crack speed under the uniaxial compression condition ranges from 0.8 to 5.3 km/s with an average value of 2.5 $\pm$ 1.4 km/s for strain rates between 71 and 1064 s^{-1}. Work in the literature has shown analytical relationships between strain-rate sensitivity of compression strength and axial crack speed [53, 59], with computational works accounting for crack speed growth in micro-mechanical models studying dynamic failure in ceramic materials [60–62]. These values are comparable yet greater when compared with previous reported crack speeds of 1.8 $\pm$ 0.6 km/s for AD-85 and 2.2 $\pm$ 0.4 km/s for AD-995 series alumina ceramics [3]. Lastly, for the reason of limited available data of crack propagation speeds on alumina, attention is extended to the ones on other brittle materials (e.g., ceramics, concrete, granite) for comparison. In the previous studies, the crack speeds were reported in a range from $\sim$ 0.3 to 0.65 km/s for sandstone [63] and $\sim$ 0.3 to 0.85 km/s for granite [64]. The crack velocities of concrete [65] were reported

as $\sim$ 1.3 km/s, while AlN ceramic [56] has a crack speed of 1.5 km/s.

For the indirect tension tests, the primary crack speed ranges from 3.1 to 10.8 km/s with the average value of 5.9 $\pm$ 2.1 km/s, while the secondary crack speed ranges from 0.4 to 3.7 km/s with the average value of 1.6 $\pm$ 0.9 km/s for strain rates ranging from 17 to 178 s^{-1}. It is observed that the computed crack speeds in this study are generally much lower than the longitudinal wave speed of $\sim$ 9870 m/s and the shear wave speed of $\sim$ 6260 m/s computed in this alumina material, with one data point from the indirect tension experiments being slightly higher (10.8 km/s). It is worth noting that the crack speed determination in this study is observational and measured from a single 2D surface of the specimen, and different factors can contribute to the scattering in data (e.g., grain morphology, interior crack initiation with later manifestation on surface, limitations in imaging). Regardless, the ratio of the measured crack speeds to the longitudinal wave speed in the current study are comparable to the limited data sets reported in the literature for brittle materials (e.g., 110% for boron carbide [66] and 98% for Mortar [67]).

Altogether, it is found that the primary crack speed in the indirect tension tests (average value of $\sim$ 5.9 km/s) is at least 2$\times$ higher than the primary speed in the compression tests (average value of $\sim$ 2.5 km/s) at a similar strain rate. The higher crack speeds in tension affect the rapid structural collapse of the sample shown previously in Figure 11 [53]. In addition, the secondary crack speed in the indirect tension tests is comparable to the ones measured under uniaxial compression, indicating a likely change in stress state to compressive during the unloading phase (see Figure 7 frame (e) and (f)). Note that the secondary cracks are often generated in conjunction with or after the primary crack has propagated across the entire specimen, and no crack branching from the primary crack is observed in the indirect tension experiments. Finally, it is also worth noting that the fracture propagation in brittle materials is a complex process that is governed by multiple factors (e.g., microstructure, stress state, strain rate, mechanical properties). It is believed that the primary crack speeds are lower in compression when compared to indirect tension experiments for the following reasons that are associated with different stages of fracture: 1. Initiation – while there is one primary crack that is initiated in indirect tension, there are a much greater number of cracks that are simultaneously initiated in compression. Therefore, the specific strain energy that is attributed to each crack under compressive loading can be lower and, thus, its speed may be lower. 2. Growth – the crack growth in indirect tension is unstable when compared with compression, where compressive crack propagation can be resisted by higher frictional forces [68]. 3. Interaction – the fewer number of cracks in indirect tension results in lower probability of interaction and coalescence, whereas the probability of interaction is much higher in compression, and this results in more opportunities for impediment (e.g., via coalescence, shielding, deflection, wave mechanics). Overall, there are few comparative measurements of compression and tension crack growth in the literature [58, 69], and so we believe our measurements can aid development of explicit fracture models describing stress-state dependent crack growth [68]. Overall, these measurements provide

21

new data for literature that are needed in development of new models describing dynamic fracture [19, 29].
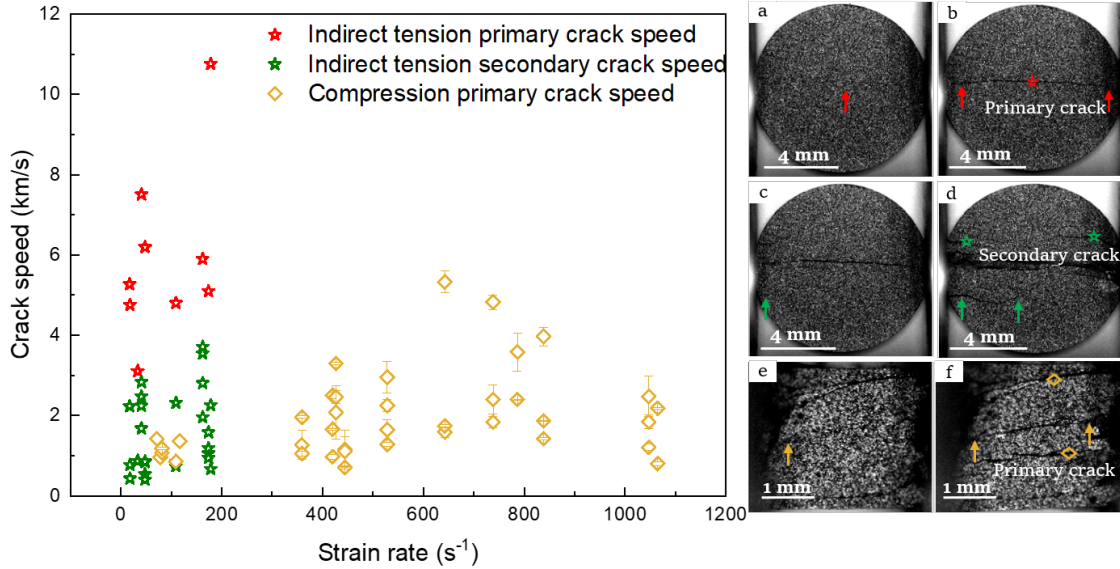
Figure 12: Crack propagation speed comparison in alumina between indirect tension and uniaxial compression experiments with ultra-high-speed images on the right. Image showing consecutive frames used to determine crack speeds in (a-d): indirect tension experiment (interframe time here of 1 µs). This experiment is at 109 s^{-1} and the frame rate is 5 Mfps. The images show that we are tracking the crack tip (shown with arrows in the sub-images) displacement over 5 to 18 consecutive frames for primary and secondary crack speed determination, respectively. In this example, the average primary and secondary crack speed are 4.8 $\pm$ 1.23 km/s and 0.84 $\pm$ 0.11 km/s. (e-f): uniaxial compression experiments (interframe time here of 0.6 µs). This experiment is at 427 s^{-1} and the frame rate is 5 Mfps. The images show that we are tracking the crack tip displacement over 3 consecutive frames. In this example, the average primary crack speed is 3.3 $\pm$ 0.58 km/s. No quasi-static experiments are plotted because the camera is not fast enough to record cracking velocities.

3.6. Post-mortem fractographic studies on fracture mechanisms

In this final Sub-section, we compare the failure behaviors (i.e., cleavage, transgranular fracture, and intergranular fracture) on surfaces of fragments retrieved from both uniaxial compression and indirect tension experiments to determine the failure mechanisms. Shown in Figure 13 are the SEM micrographs showing the fracture mechanisms of the alumina under quasi-static loading: (a1) - (a2) for uniaxial compression, (b1) - (b2) for indirect tension, and for dynamic experiments: (c1) - (c2) for uniaxial compression, (d1) - (d2) for indirect tension. In Figure 13 (a1), the fracture surface of the quasi-static uniaxial compression experiments shows multiple microcracks spanning across the field of view (see orange dashed lines). Figure 13 (a2) shows a magnified view at a triple junction of cracks crossing numerous grains on a flat fracture plane. The relative roughness of the fracture plane suggests that intergranular fracture is likely dominant under quasi-static compressive loading. Similarly, Figure 13 (b1) presents a fracture surface taken on the fragment from the quasi-static indirect tension experiment, and this demonstrates that pores (see green arrows) and cleavages

22

(see orange arrows) appeared on large flat grain surfaces, and rough fracture planes which are full of sharp
edges indicates that the crack propagated along grain boundaries (i.e., intergranular fracture). In Figure 13
(b2) for the quasi-static tensile condition, a triple junction (see the blue arrow) contained within a few
grains is identified. Note that the occurrence of intergranular frature is likely related to the relatively weak
interfacial strength at the grain boundary [16]. In summary, it is observed that intergranular fracture with
cracks propagating along the grain boundaries is the more dominant fracture mode under quasi-static loading
in both compressive and tensile conditions. A similar phenomenon was observed for alumina fragments with
uneven and sharp edges under quasi-static compression by Wang et al. [16].

Next, Figure 13 (c1) shows the fracture surface for the dynamic compression condition with microcracks
propagating across the field of view with a mixed-mode of intergranular and transgranular fracture (see red
arrows). Figure 13 (c2) presents a magnified view focusing on a large flat grain surface showing extensive
cleavages (see the orange arrow), and this is often thought to be a consequence of local twist and plane damage
propagation [70]. In Figure 13 (d1), a global view of the fracture plane taken from dynamic indirect tension
experiments with a large percentage of flat grains (see red dashed circles) is observed, and this indicates
transgranular fracture as the dominant failure mechanism. Next, Figure 13 (d2) shows a magnified view
on the flat grain areas (see red dashed circles) with secondary transgranular cracks (see the orange arrow)
spanning across the grains. Overall, by comparing different stress states, we found that more cracks are likely
to appear in uniaxial compression experiments (see Figure 13 (a) and (c)) when compared to the indirect
tension experiments (see Figure 13 (b) and (d)). This agrees with the experimental observations using high-
speed imaging (see Figure 6 and Figure 7) that few primary cracks in the indirect tension experiments often
initiate and grow along the mid-plane of the specimen, with less number of fragments generated after complete
failure (i.e., two half-disk large fragments can usually be retrieved). On the other hand, numerous primary
cracks (i.e., axial splitting) can be generated simultaneously during compressive loading with secondary
cracks and crack-crack interactions following. Under compressive loading, fragments are usually powder-like,
as is commonly observed in the literature [71]. Lastly, by comparing Figure 13 (a) and (b) to Figure 13
(c) and (d) across different loading rates, it is observed that dynamic loading rates lead to an increase in
transgranular fracture, which has been noted before in the literature [16]. More extensive cleavages are also
found when the loading condition is dynamic. Lastly, spherical porosity features are observed generally on all
the examined fracture surfaces (features noted in (b1) but not in others due to space), although no evidence
is observed in Figure 13 that these spherical features have microcracks emanating from them.

Finally, a comparison between compressive and tensile behaviors of the studied alumina and cited ceramics
is summarized. Firstly, as commonly known about brittle materials, the strength in compression is much
higher than those in tension, which is $>10\times$ in the current alumina (Figure 9). This trend is related to the
initiation growth and coalescence of cracks [53], as observed in Figure 13. Secondly, the strain-rate-sensitivity
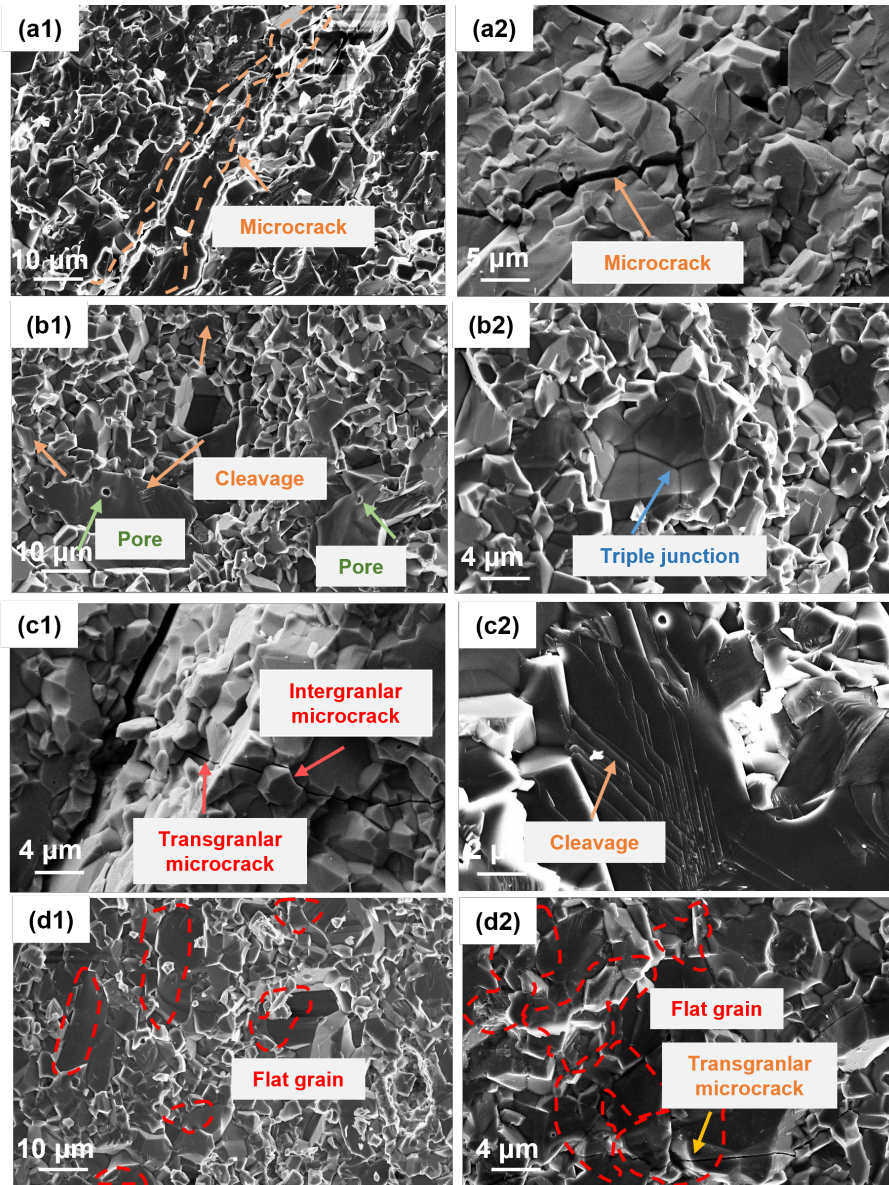
Figure 13: SEM micrograph showing the fractography of the 98% alumina under quasi-static loading (a for uniaxial compression, b for indirect tension) and dynamic loading (c for uniaxial compression, d for indirect tension). (a1) Fracture surface showing cracks spanning across the field of view, where multiple cracks can be observed (see red dashed line). (a2) A magnified view of a triple junction of cracks crossing numerous grains on a flat fracture plane. The flatness of the fracture plane indicates transgranular fracture. (b1) Fracture surface showing pores and cleavages with a rough fracture plane, the rough fracture plane indicates intergranular fracture. (b2) A magnified view of a triple junction that is limited within a few grains. (c1) Fracture surface showing cracks propagating across the field of view with a mixed-mode of intergranular and transgranular fracture. (c2) A typical view of a fracture surface showing extensive cleavage of alumina. (d1) A global view of the fracture plane with large regions of flat grains indicating transgranular fracture as the dominant failure mechanism. (d2) A magnified view on the flat grain areas with secondary transgranular cracks spanning across the grains.

24

of strength on compression is greater than that on tension under dynamic loading. This behavior is believed to be associated with the crack nucleation (Figure 12), and its growth and interactions (Figure 11) which is still difficult to clarify clearly. Specifically, under compression loading, the crack growth is inherently stable until the crack interactions dominate the failure, thus the influence of increasing the strain rate on the activation of flaws is greater than that in the tension cases [53]. While under a tensile stress state, a few unstable crack growth with much higher speeds often dominate the fracture process. To date, limited experimental data on both compressive and tensile tests have been reported, and, thus, this paper serves to make contributions to these understandings.

4. Conclusions

The current study investigates the mechanical behaviors and failure mechanisms of a CeramTec Alotec 98% alumina under uniaxial compression and indirect tension loading both under quasi-static and dynamic conditions. The conclusions have been drawn as follows:

1. The microstructural features (e.g., elemental composition, grain size, voids and impurities) of the CeramTec Alotec 98% alumina is determined with multiple techniques (e.g., SEM coupled with EDS, EBSD, and XRM), and are associated with greater strength of the material relative to previous literature.

2. The validity of the uniaxial compression and indirect tension experiments are provided through DIC analysis. For compression experiments, overlapping of strain-time from all AOIs and stress-time curves demonstrates the goodness of the experiments. For indirect tension experiments, the phenomenon of low shear strain, crack initiation in the middle, and a good symmetry in displacement between the upper and lower half of the specimen show the validity of our approach and specimen design.

3. The peak strength of the material in compression (ranging from 2467 to 3916 MPa) is $>10\times$ higher than those in tension (ranging from 282 to 320 MPa), which is ascribed to the physics of the initiation, growth, and coalescence of cracks [19].

4. Both the uniaxial compression and indirect tension strength of the CeramTec Alotec 98% alumina showed strain rate sensitivitywith the compression (linear slope fit of 0.68) being greater than in tension (linear slope fit of 0.39). Additionally, Young's modulus shows no obvious stress-state- and strain-rate-dependency.

5. The primary crack speed measurements show an average of 5.9 $\pm$ 2.1 km/s for uniaxial compression tests and 2.5 $\pm$ 1.4 km/s for indirect tension tests. The secondary crack speed measurements of the indirect tension tests show an average of 1.6 $\pm$ 0.9 km/s, which is comparable to the primary crack

25

speed under uniaxial compression $(2.5 \pm 1.4 \, \text{km/s})$. This comparable crack speed is likely a consequence of the shift in stress state from tensile to compressive during failure.

6. Post-mortem analysis revealed that transgranular fracture dominates the dynamic failure process, and intergranular fracture dominates quasi-static failure. More micro-cracking is observed under compressive loading than in tension.

5. Acknowledgment

References

[1] J. Chen, B. Guo, H. Liu, H. Liu, P. Chen, Dynamic brazilian test of brittle materials using the split hopkinson pressure bar and digital image correlation, Strain 50 (6) (2014) 563–570.

[2] M. Scapin, L. Peroni, M. Avalle, Dynamic brazilian test for mechanical characterization of ceramic ballistic protection, Shock and Vibration 2017 (2017).

[3] B. M. Koch, P. Jannotti, D. Mallick, B. Schuster, T. Sano, J. D. Hogan, Influence of microstructure on the impact failure of alumina, Materials Science and Engineering: A 770 (2020) 138549.

[4] Q. Wang, X. Jia, S. Kou, Z. Zhang, P.-A. Lindqvist, The flattened brazilian disc specimen used for testing elastic modulus, tensile strength and fracture toughness of brittle rocks: analytical and numerical results, International Journal of Rock Mechanics and Mining Sciences 41 (2) (2004) 245–253.

[5] S. Acharya, S. Bysakh, V. Parameswaran, A. K. Mukhopadhyay, Deformation and failure of alumina under high strain rate compressive loading, Ceramics International 41 (5) (2015) 6793–6801.

[6] J. Lankford, Mechanisms responsible for strain-rate-dependent compressive strength in ceramic materials, Journal of the American Ceramic Society 64 (2) (1981) C–33.

[7] B. Amirian, H. Li, J. Hogan, The mechanical response of a $\alpha2$ (ti3al)+ γ (tial)-submicron grained al2o3 cermet under dynamic compression: Modeling and experiment, Acta Materialia 181 (2019) 291–308.

[8] F. Gálvez, J. Rodríguez, V. S. Gálvez, Influence of the strain rate on the tensile strength in aluminas of different purity, Le Journal de Physique IV 10 (PR9) (2000) Pr9–323.

[9] A. Tiamiyu, R. Basu, A. Odeshi, J. A. Szpunar, Plastic deformation in relation to microstructure and texture evolution in aa 2017-t451 and aa 2624-t351 aluminum alloys under dynamic impact loading, Materials Science and Engineering: A 636 (2015) 379–388.

[10] G. Hu, J. Liu, L. Graham-Brady, K. Ramesh, A 3d mechanistic model for brittle materials containing evolving flaw distributions under dynamic multiaxial loading, Journal of the Mechanics and Physics of Solids 78 (2015) 269–297.

[11] B. Paliwal, K. T. Ramesh, J. W. McCauley, M. Chen, Dynamic compressive failure of alon under controlled planar confinement, Journal of the American Ceramic Society 91 (11) (2008) 3619–3629.

[12] H. Li, P. Motamedi, J. Hogan, Characterization and mechanical testing on novel $(\gamma+ \alpha2)$–tial/ti3al/al2o3 cermet, Materials Science and Engineering: A 750 (2019) 152–163.

[13] P. Gehre, C. Aneziris, Ebsd-and ct-analyses for phase evolution and crack investigations of thermal shocked flame sprayed alumina and alumina-rich structures, Ceramics International 37 (6) (2011) 1731–1737.

[14] Z. Wang, P. Li, Characterisation of dynamic behaviour of alumina ceramics: evaluation of stress uniformity, AIP Advances 5 (10) (2015) 107224.

[15] S. Dong, K. Xia, S. Huang, T. Yin, Rate dependence of the tensile and flexural strengths of glass–ceramic macor, Journal of Materials Science 46 (2) (2011) 394–399.

[16] Z. Wang, P. Li, Dynamic failure and fracture mechanism in alumina ceramics: Experimental observations and finite element modelling, Ceramics International 41 (10) (2015) 12763–12772.

[17] J. Venkatesan, M. Iqbal, V. Madhu, Experimental and numerical study of the dynamic response of b4c ceramic under uniaxial compression, Thin-Walled Structures 154 (2020) 106785.

[18] Y. Gao, T. Tang, C. Yi, W. Zhang, D. Li, W. Xie, W. Huang, N. Ye, Study of static and dynamic behavior of tib2–b4c composite, Materials & Design 92 (2016) 814–822.

[19] K. Ramesh, J. D. Hogan, J. Kimberley, A. Stickle, A review of mechanisms and models for dynamic failure, strength, and fragmentation, Planetary and Space Science 107 (2015) 10–23.

[20] S. Xu, J. Huang, P. Wang, C. Zhang, L. Zhou, S. Hu, Investigation of rock material under combined compression and shear dynamic loading: an experimental technique, International Journal of Impact Engineering 86 (2015) 206–222.

[21] M. Z. Sheikh, Z. Wang, B. Du, T. Suo, Y. Li, F. Zhou, Y. Wang, U. A. Dar, G. Gao, Y. Wang, Static and dynamic brazilian disk tests for mechanical characterization of annealed and chemically strengthened glass, Ceramics International 45 (6) (2019) 7931–7944.

[22] C. Johnstone, C. Ruiz, Dynamic testing of ceramics under tensile stress, International Journal of Solids and Structures 32 (17-18) (1995) 2647–2656.

[23] I. S. for Rock Mechanics. Commission on Standardization of Laboratory, F. T. C. on Laboratory Tests, Suggested methods for determining tensile strength of rock materials, The Society, 1977.

[24] J. J. Swab, J. Yu, R. Gamble, S. Kilczewski, Analysis of the diametral compression method for determining the tensile strength of transparent magnesium aluminate spinel, International journal of fracture 172 (2) (2011) 187–192.

[25] Q.-Z. Wang, L. Xing, Determination of fracture toughness kic by using the flattened brazilian disk specimen for rocks, Engineering fracture mechanics 64 (2) (1999) 193–201.

28

[26] R. Chen, F. Dai, J. Qin, F. Lu, Flattened brazilian disc method for determining the dynamic tensile stress-strain curve of low strength brittle solids, Experimental Mechanics 53 (7) (2013) 1153–1159.

[27] C. Cady, G. Gray III, Influence of strain rate on the deformation and fracture response of a 6061-t6 al–50 vol.% al2o3 continuous-reinforced composite, Materials Science and Engineering: A 298 (1-2) (2001) 56–62.

[28] C. Y. Rena, G. Ruiz, A. Pandolfi, Numerical investigation on the dynamic behavior of advanced ceramics, Engineering Fracture Mechanics 71 (4-6) (2004) 897–911.

[29] A. L. Tonge, J. Kimberley, K. Ramesh, A consistent scaling framework for simulating high rate brittle failure problems, Procedia Engineering 58 (2013) 692–701.

[30] B. M. Koch, C. Lo, H. Li, T. Sano, J. Ligda, J. D. Hogan, Dynamic mechanical response of damaged alumina ad995, Journal of the European Ceramic Society 41 (3) (2021) 2034–2048.

[31] J. Swab, W. Chen, J. Hogan, H. Liao, C. Lo, S. Mates, C. Meredith, J. Pittari, R. Rhorer, G. Quinn, Dynamic compression strength of ceramics: What was learned from an interlaboratory round robin exercise?, Journal of Dynamic Behavior of Materials 7 (1) (2021) 34–47.

[32] J. Lankford, W. Predebon, J. Staehler, G. Subhash, B. Pletka, C. Anderson, The role of plasticity as a limiting factor in the compressive failure of high strength ceramics, Mechanics of Materials 29 (3-4) (1998) 205–218.

[33] J. Staehler, W. Predebon, B. Pletka, G. Subhash, Micromechanisms of deformation in high-purity hot-pressed alumina, Materials Science and Engineering: A 291 (1-2) (2000) 37–45.

[34] H. Luo, W. Chen, Dynamic compressive response of intact and damaged ad995 alumina, International Journal of Applied Ceramic Technology 1 (3) (2004) 254–260.

[35] W. Huang, M. Wang, Z. Hu, L. Wang, J. Cao, D. Kong, Experimental and numerical investigation on strain rate-dependent tensile behavior of zrb2-sic ceramic composite, Acta Mechanica Solida Sinica 34 (1) (2021) 137–148.

[36] H. Lin, W. Xiong, Q. Yan, Modified formula for the tensile strength as obtained by the flattened brazilian disk test, Rock Mechanics and Rock Engineering 49 (4) (2016) 1579–1586.

[37] A. Griffith, Proceedings of the first international congress on applied mechanics, Delft. J. Waltman Jr, Delft (1924) 55–63.

[38] C. Lo, T. Sano, J. D. Hogan, Microstructural and mechanical characterization of variability in porous advanced ceramics using x-ray computed tomography and digital image correlation, Materials Characterization 158 (2019) 109929.

[39] W. Chen, G. Ravichandran, Dynamic compressive failure of a glass ceramic under lateral confinement, Journal of the Mechanics and Physics of Solids 45 (8) (1997) 1303–1328.

[40] N. Muskhelishvili, Some basic problems of the mathematical theory of elasticity, Noordhoff, Groningen 17404 (6.2) (1963) 1.

[41] X. Jin, C. Hou, X. Fan, C. Lu, H. Yang, X. Shu, Z. Wang, Quasi-static and dynamic experimental studies on the tensile strength and failure pattern of concrete and mortar discs, Scientific reports 7 (1) (2017) 1–15.

[42] S.-W. Khoo, S. Karuppanan, C.-S. Tan, A review of surface deformation and strain measurement using two-dimensional digital image correlation, Metrology and Measurement Systems 23 (3) (2016).

[43] B. Pan, K. Qian, H. Xie, A. Asundi, Two-dimensional digital image correlation for in-plane displacement and strain measurement: a review, Measurement science and technology 20 (6) (2009) 062001.

[44] R. Panowicz, M. Konarzewski, Influence of imperfect position of a striker and input bar on wave propagation in a split hopkinson pressure bar (shpb) setup with a pulse-shape technique, Applied Sciences 10 (7) (2020) 2423.

[45] P. Chantikul, S. J. Bennison, B. R. Lawn, Role of grain size in the strength and r-curve properties of alumina, Journal of the American Ceramic Society 73 (8) (1990) 2419–2427.

[46] G. Le, A. Godfrey, N. Hansen, Structure and strength of aluminum with sub-micrometer/micrometer grain size prepared by spark plasma sintering, Materials & Design 49 (2013) 360–367.

[47] S. J. Dillon, M. P. Harmer, Demystifying the role of sintering additives with "complexion", Journal of the European Ceramic Society 28 (7) (2008) 1485–1493.

[48] V. Nečina, W. Pabst, Influence of the heating rate on grain size of alumina ceramics prepared via spark plasma sintering (sps), Journal of the European Ceramic Society 40 (10) (2020) 3656–3662.

[49] R. Benitez, H. Gao, M. O'Neal, P. Lovelace, G. Proust, M. Radovic, Effects of microstructure on the mechanical properties of ti2alc in compression, Acta Materialia 143 (2018) 130–140.

[50] A. Belenky, D. Rittel, Static and dynamic flexural strength of 99.5% alumina: relation to porosity, Mechanics of Materials 48 (2012) 43–55.

[51] C. E. Anderson Jr, S. A. Royal-Timmons, Ballistic performance of confined 99.5%-al2o3 ceramic tiles, International journal of impact engineering 19 (8) (1997) 703–713.

[52] C. Lo, T. Sano, J. D. Hogan, Deformation mechanisms and evolution of mechanical properties in damaged advanced ceramics, Journal of the European Ceramic Society 40 (8) (2020) 3129–3139.

[53] J. Kimberley, K. Ramesh, N. Daphalapurkar, A scaling law for the dynamic strength of brittle solids, Acta Materialia 61 (9) (2013) 3509–3521.

[54] C. A. Ross, J. W. Tedesco, S. T. Kuennen, Effects of strain rate on concrete strength, Materials Journal 92 (1) (1995) 37–47.

[55] T. Fu, X. Peng, C. Huang, S. Weng, Y. Zhao, Z. Wang, N. Hu, Strain rate dependence of tension and compression behavior in nano-polycrystalline vanadium nitride, Ceramics International 43 (15) (2017) 11635–11641.

[56] G. Hu, K. Ramesh, B. Cao, J. McCauley, The compressive failure of aluminum nitride considered as a model advanced ceramic, Journal of the Mechanics and Physics of Solids 59 (5) (2011) 1076–1093.

[57] J. Schukraft, C. Lohr, K. A. Weidenmann, 2d and 3d in-situ mechanical testing of an interpenetrating metal ceramic composite consisting of a slurry-based ceramic foam and alsi10mg, Composite Structures 263 (2021) 113742.

[58] V. Kannan, K. Hazeli, K. Ramesh, The mechanics of dynamic twinning in single crystal magnesium, Journal of the Mechanics and Physics of Solids 120 (2018) 154–178.

[59] C. C. Holland, R. M. McMeeking, The influence of mechanical and microstructural properties on the rate-dependent fracture strength of ceramics in uniaxial compression, International Journal of Impact Engineering 81 (2015) 34–49.

[60] W. Li, K. Ramesh, A finite deformation framework for mechanism-based constitutive models of the dynamic behavior of brittle materials, Journal of the Mechanics and Physics of Solids 155 (2021) 104518.

[61] A. L. Tonge, K. Ramesh, Multi-scale defect interactions in high-rate brittle material failure. part i: Model formulation and application to alon, Journal of the Mechanics and Physics of Solids 86 (2016) 117–149.

[62] A. L. Tonge, J. Kimberley, K. Ramesh, The mechanism of compressive unloading failure in single crystal quartz and other brittle solids, International Journal of Solids and Structures 49 (26) (2012) 3923–3934.

[63] Q. B. Zhang, J. Zhao, Quasi-static and dynamic fracture behaviour of rock materials: phenomena and mechanisms, International Journal of Fracture 189 (1) (2014) 1–32.

[64] R. Chen, K. Xia, F. Dai, F. Lu, S. Luo, Determination of dynamic fracture parameters using a semi-circular bend technique in split hopkinson pressure bar testing, Engineering Fracture Mechanics 76 (9) (2009) 1268–1276.

[65] P. Forquin, An optical correlation technique for characterizing the crack velocity in concrete, The European Physical Journal Special Topics 206 (1) (2012) 89–95.

[66] M. Shaeffer, J. D. Hogan, L. Farbaniec, K. Ramesh, Determination of dynamic tensile strength in boron carbide using the brazilian disk method.

[67] F. Yang, H. Ma, L. Jing, L. Zhao, Z. Wang, Dynamic compressive and splitting tensile tests on mortar using split hopkinson pressure bar technique, Latin American Journal of Solids and Structures 12 (2015) 730–746.

[68] Q. H. Zuo, F. L. Addessio, J. K. Dienes, M. W. Lewis, A rate-dependent damage model for brittle materials based on the dominant crack, International Journal of Solids Structures 43 (11–12) (2006) 3350–3380.

[69] H. Li, C. Shao, D. F. Rojas, M. Ponga, J. D. Hogan, Micro-hardness and strain-rate-dependent compressive response of an ultra-light-weight mg-li-al alloy, Journal of Alloys and Compounds 890 (2022) 161703.

[70] A. K. Mukhopadhyay, K. D. Joshi, A. Dey, R. Chakraborty, A. Rav, S. K. Biswas, S. C. Gupta, Shock deformation of coarse grain alumina above hugoniot elastic limit, Journal of materials science 45 (13) (2010) 3635–3651.

[71] J. D. Hogan, L. Farbaniec, T. Sano, M. Shaeffer, K. Ramesh, The effects of defects on the uniaxial compressive strength and failure of an advanced ceramic, Acta Materialia 102 (2016) 263–272.